Supporting Information for

N-Substituted Derivatives of the Azadithiolate Cofactor from the [FeFe]-Hydrogenases: Stability and Complexation

Raja Angamuthu, Chi-Shian Chen, Tyler R. Cochrane, Danielle L. Gray, David Schilter, Olbelina A. Ulloa, and Thomas B. Rauchfuss*

School of Chemical Sciences, University of Illinois at Urbana-Champaign, Urbana, IL 61801, USA

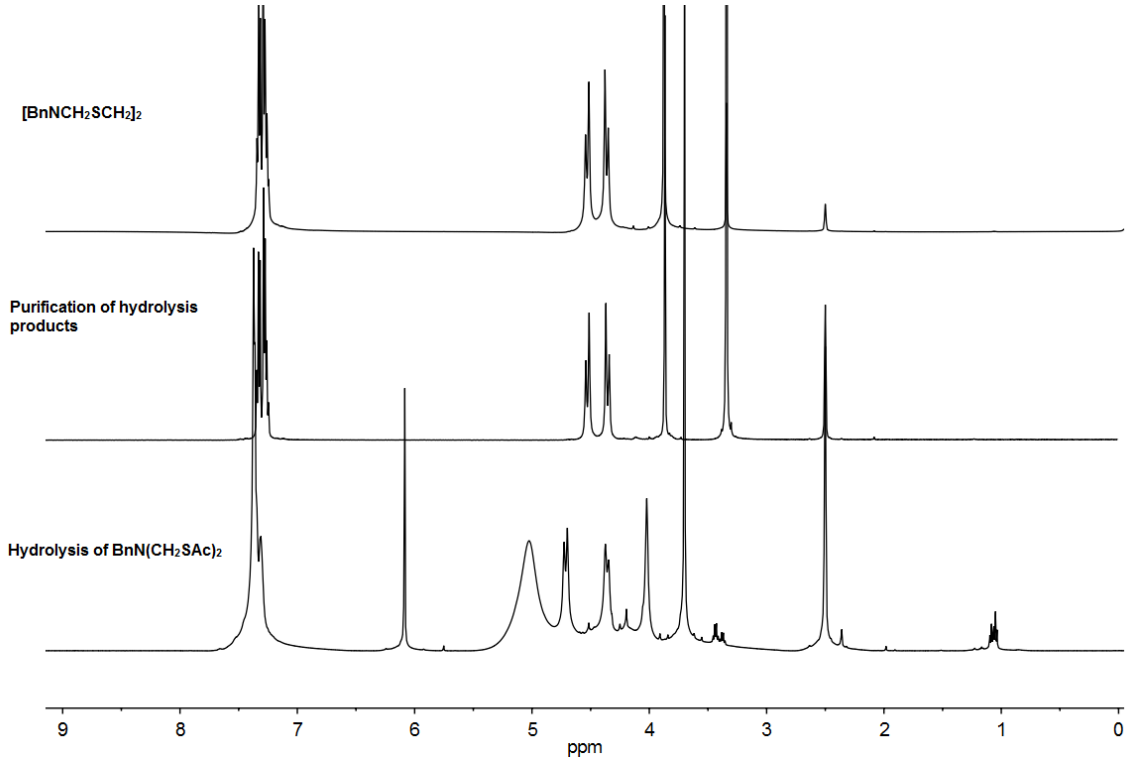

Figure S1. ^{1}H NMR spectra (DMSO-d_6, 500 MHz) of $[BnNCH_2SCH_2]_2$ obtained from hydrolysis of $BnN(CH_2SAc)_2$ (bottom, middle) and from condensation of $BnNH_2$, CH_2O, and $NaSH{\cdot}xH_2O$ (top). The signals at δ2.50, 3.33, and 3.71 are for DMSO-d_5, H_2O, and 1,3,5-trimethoxybenzene (integration standard), respectively.

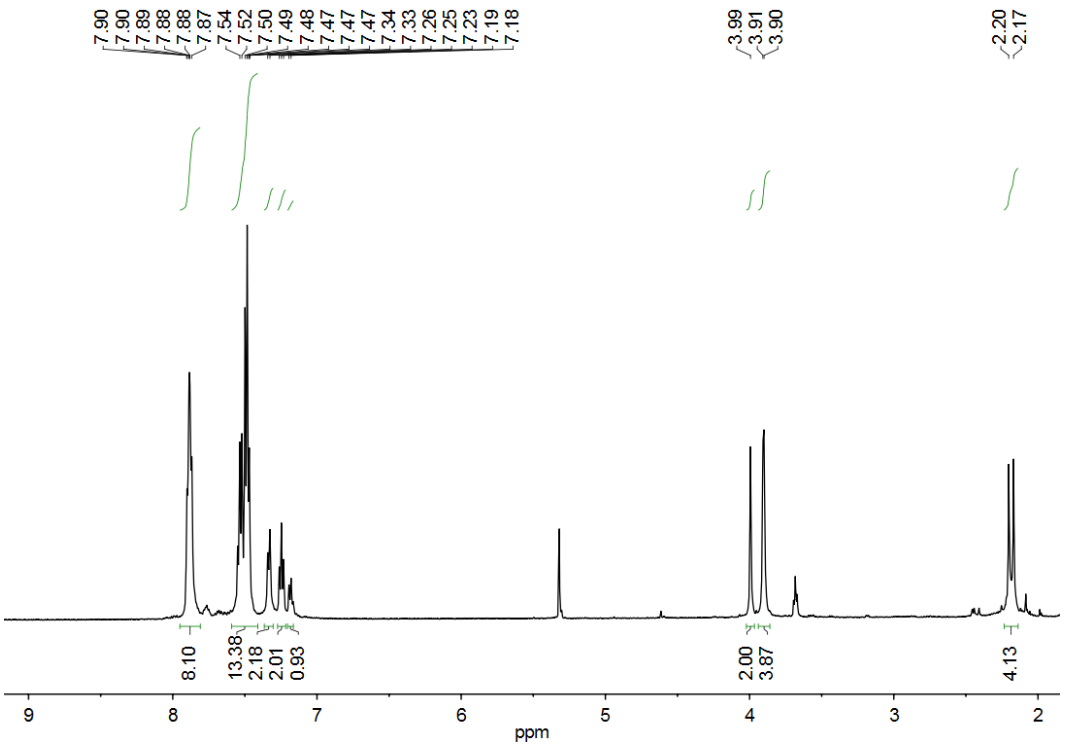

Figure S2. ^{1}H NMR spectrum (CD_2Cl_2, 500 MHz) of Ni[$(SCH_2)_2$NBn](dppe). The resonances at δ5.32 and 3.69 are for $CHDCl_2$ and THF, respectively.

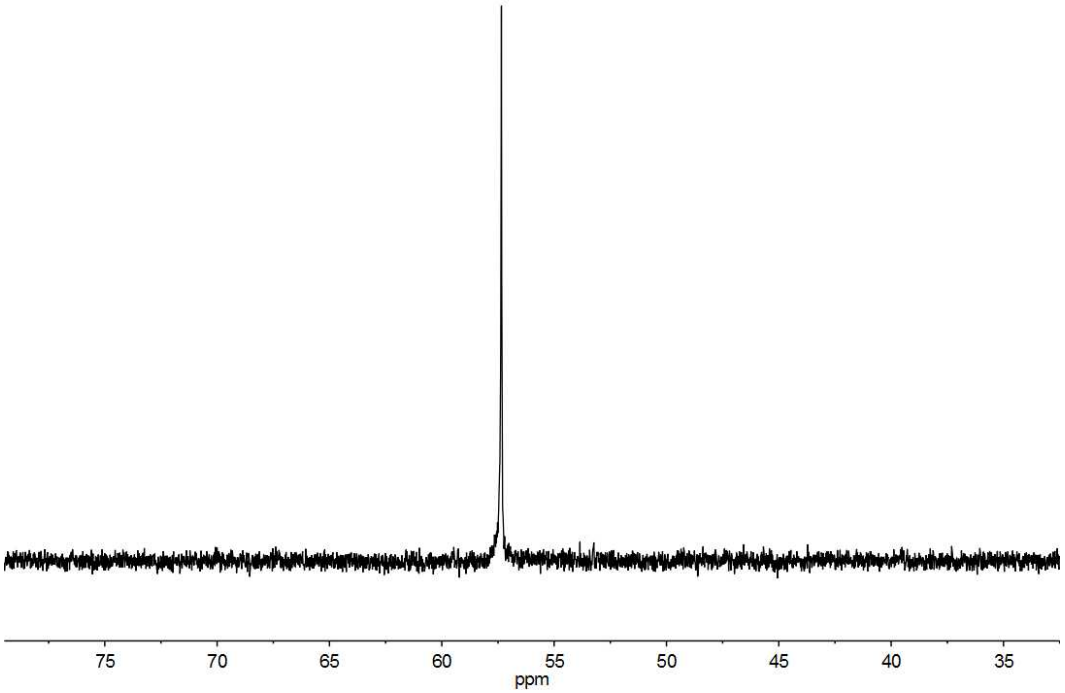

Figure S3. $^{31}P\{^{1}H\}$ NMR spectrum (CD_2Cl_2, 202 MHz) of Ni[$(SCH_2)_2$NBn](dppe).

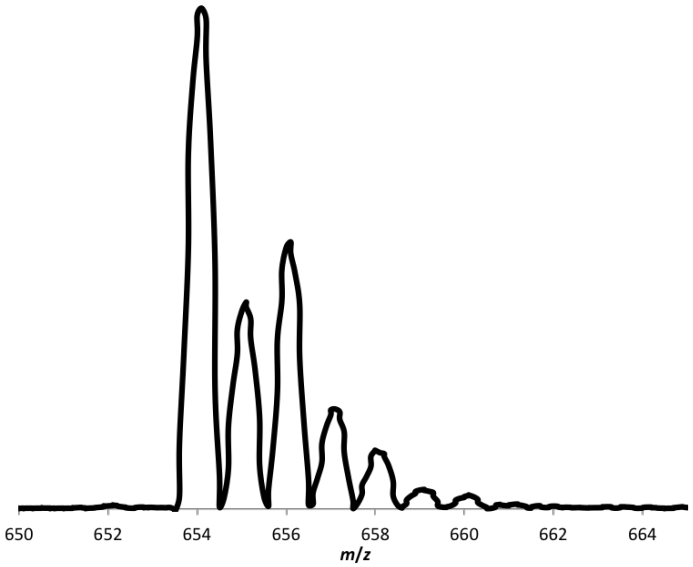

Figure S4. Positive ion ESI mass spectrum of Ni[$(SCH_2)_2$NBn](dppe).

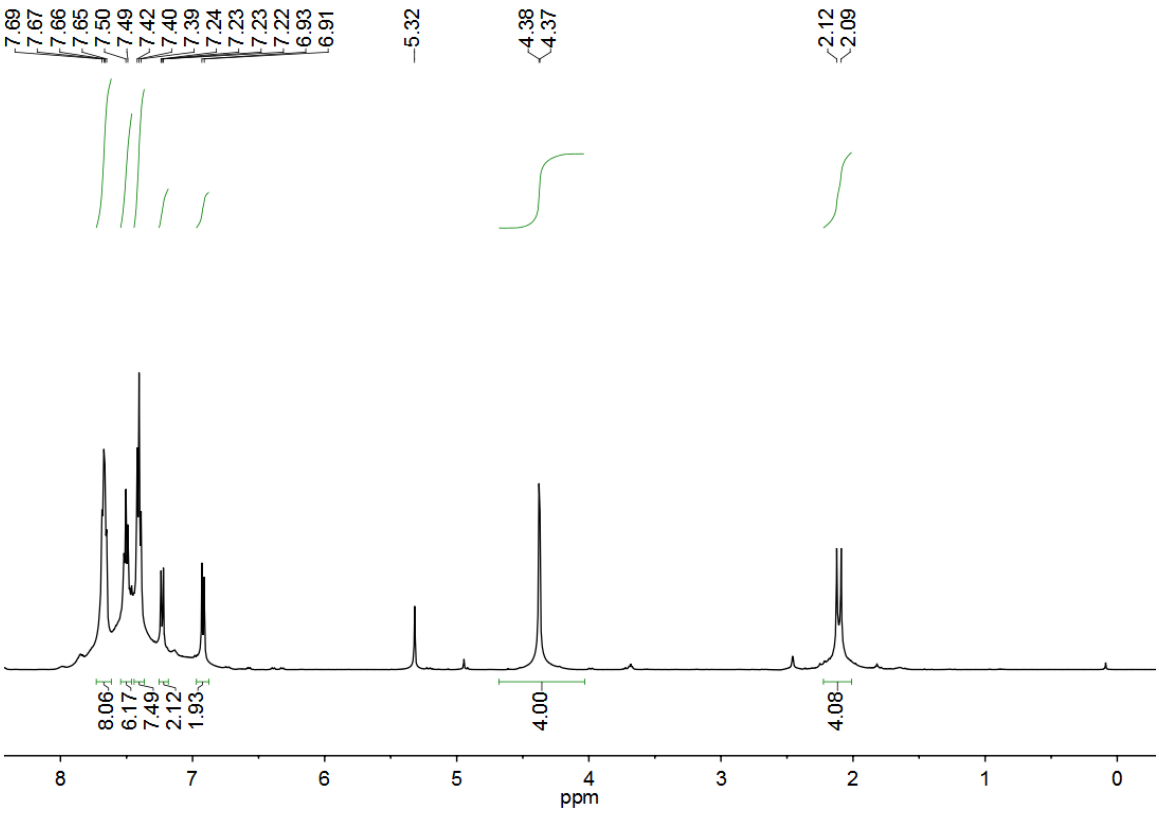

Figure S5. ^{1}H NMR spectrum (CD_2Cl_2, 500 MHz) of Ni[$(SCH_2)_2NC_6H_4Cl$](dppe). The resonances at δ5.32 and 3.69 are for $CHDCl_2$ and THF, respectively.

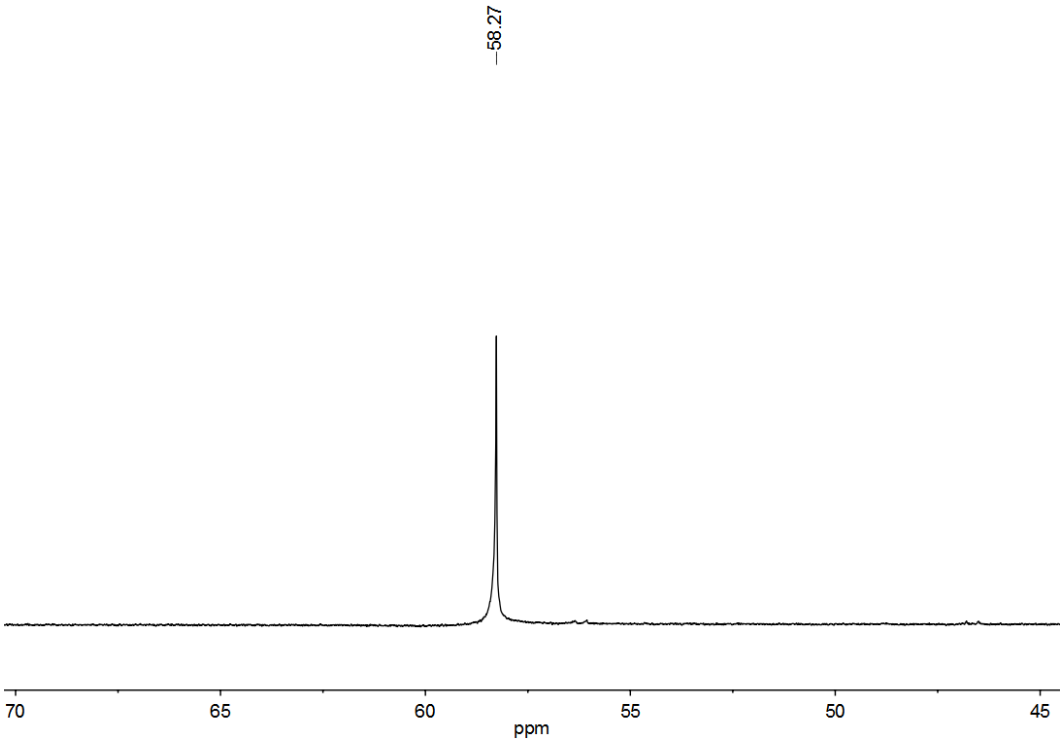

Figure S6. $^{31}P\{^{1}H\}$ NMR spectrum (CD_2Cl_2, 202 MHz) of $Ni[(SCH_2)_2NC_6H_4Cl](dppe)$.

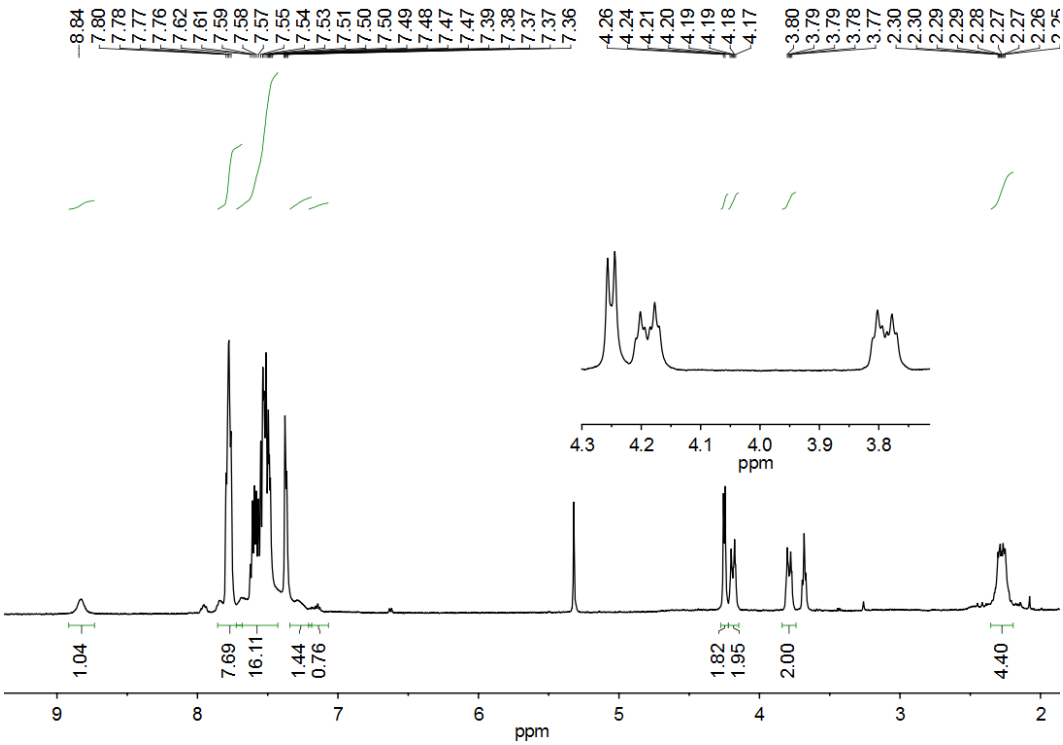

Figure S7. ^{1}H NMR spectrum (CD_2Cl_2, 500 MHz) of $[Ni[(SCH_2)_2N(H)Bn](dppe)]OTf$. The resonances at δ5.32 and 3.69 are for $CHDCl_2$ and THF, respectively.

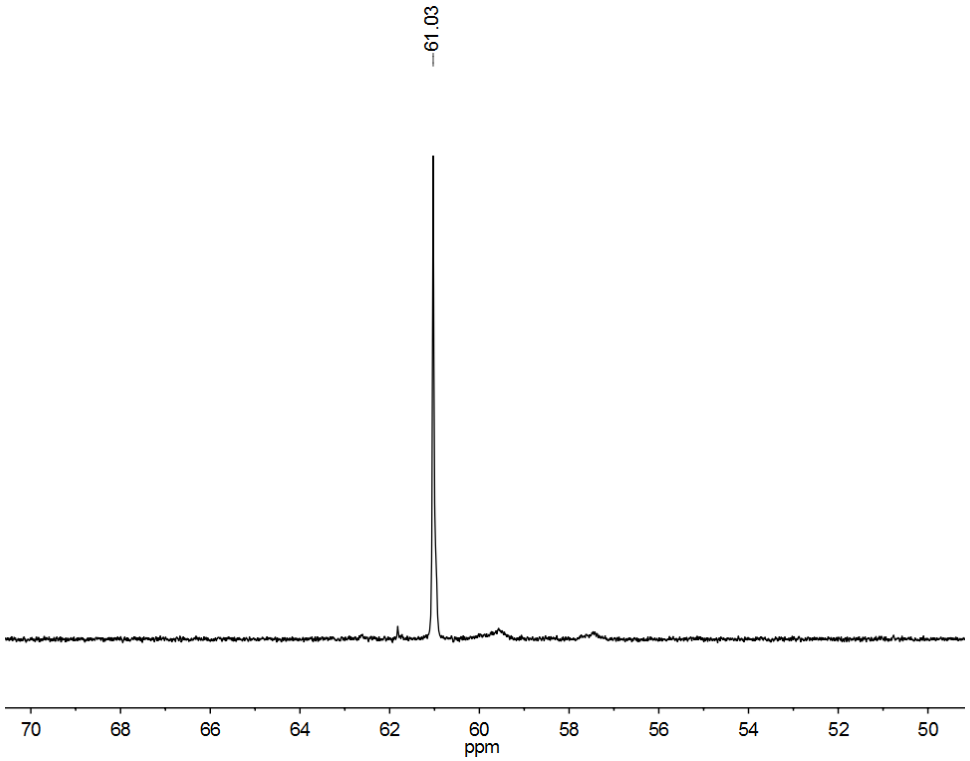

Figure S8. $^{31}P\{^{1}H\}$ NMR spectrum (CD_2Cl_2, 202 MHz) of [Ni[$(SCH_2)_2N(H)Bn$](dppe)]OTf.

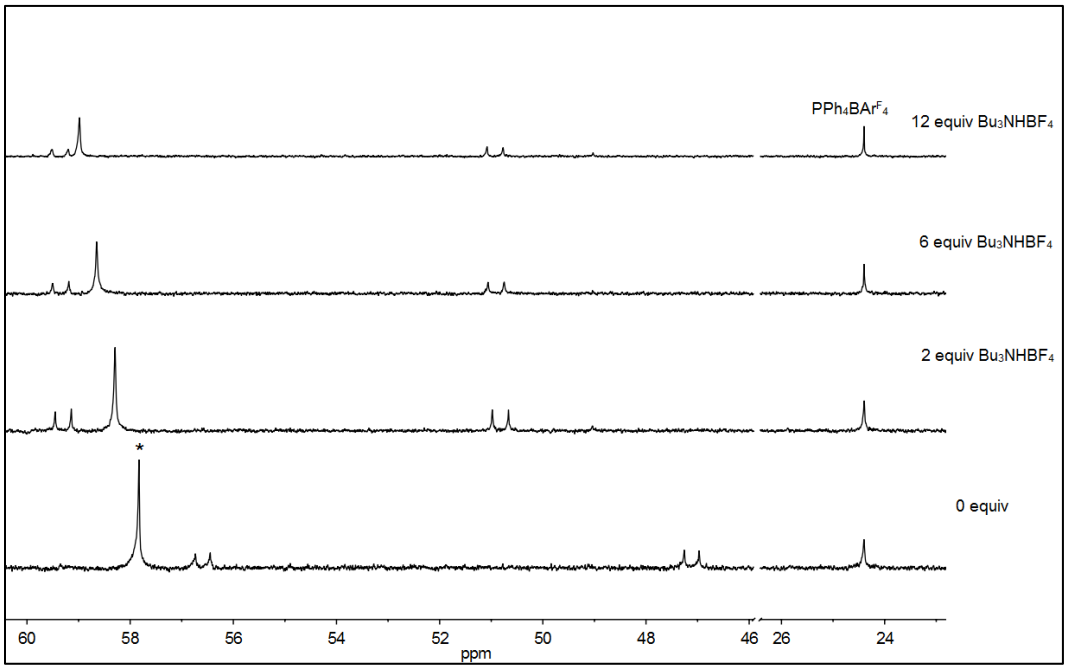

Figure S9. $^{31}P\{^{1}H\}$ NMR spectrum (CD_2Cl_2, 202 MHz) of Ni[$(SCH_2)_2NBn$](dppe) with increasing amounts of Bu_3NHBF_4 in the presence of the internal standard $PPh_4BAr^F_4$ in MeCN. * refers to Ni[$(SCH_2)_2NBn$](dppe). The signals at δ45 and δ54 are unassigned contaminant.

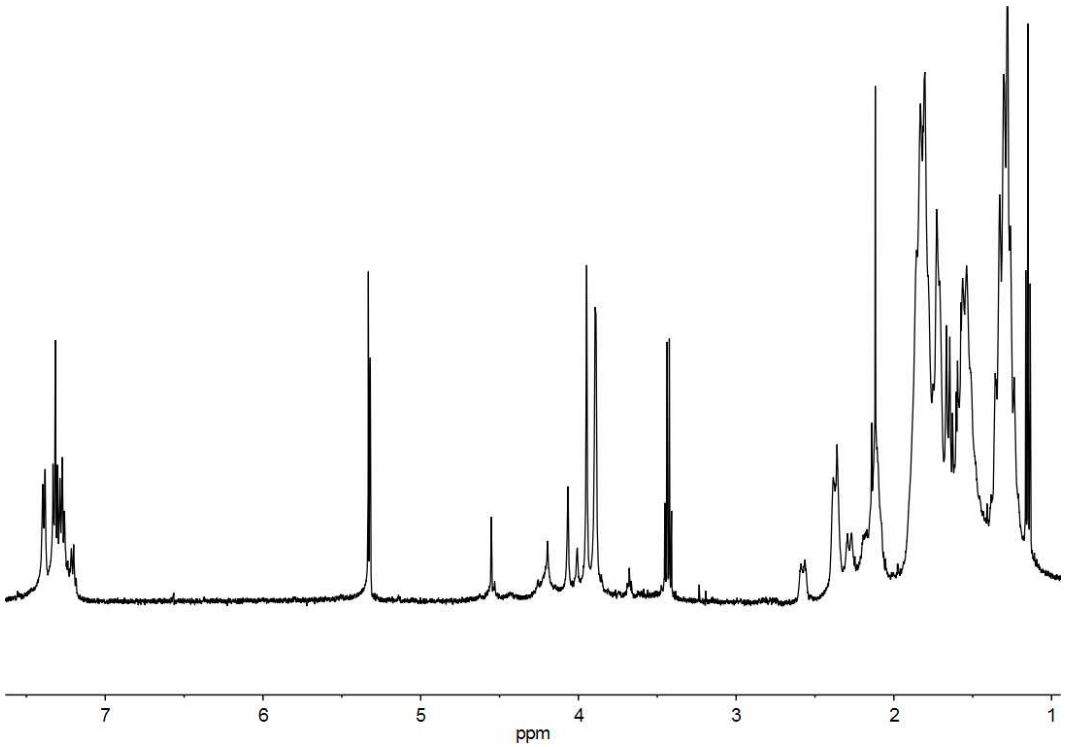

Figure S10. ^{1}H NMR spectrum (CD_2Cl_2, 500 MHz) of crude Ni[$(SCH_2)_2$NBn](dcpe). The resonances at δ5.32 ($CHDCl_2$), 3.69 (THF), 3.43 (Et_2O), 1.30 (pentane) and 1.15 (Et_2O) are from solvent impurities.

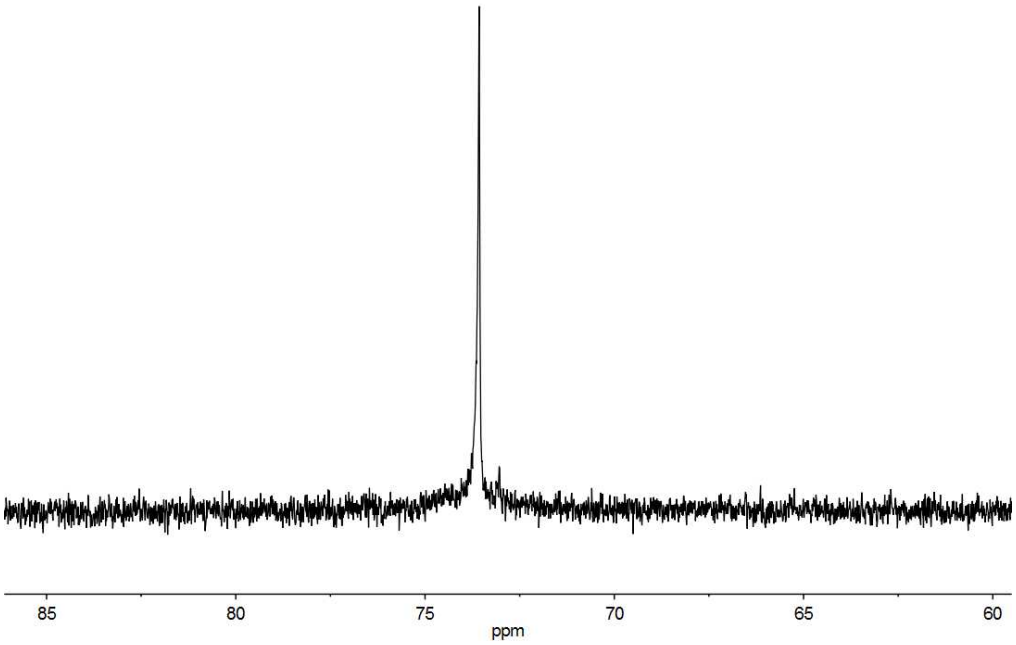

Figure S11. $^{31}P\{^{1}H\}$ NMR spectrum (CD_2Cl_2, 202 MHz) of crude Ni[$(SCH_2)_2$NBn](dcpe).

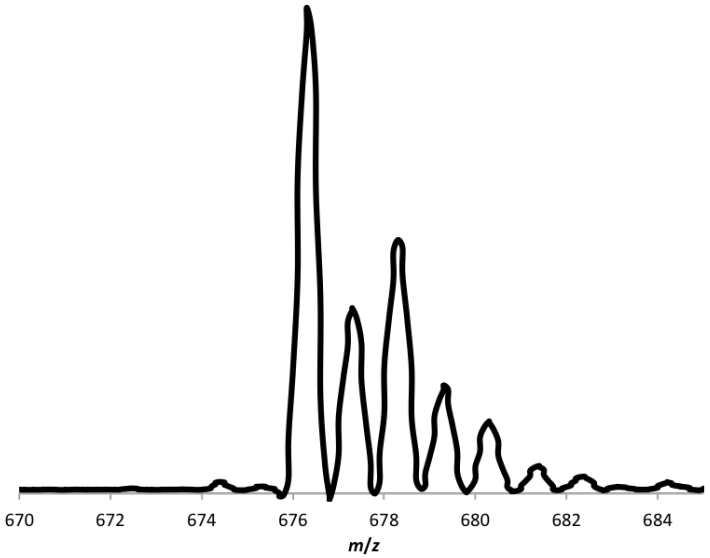

Figure S12. Positive ion ESI mass spectrum of Ni[$(SCH_2)_2$NBn](dcpe).

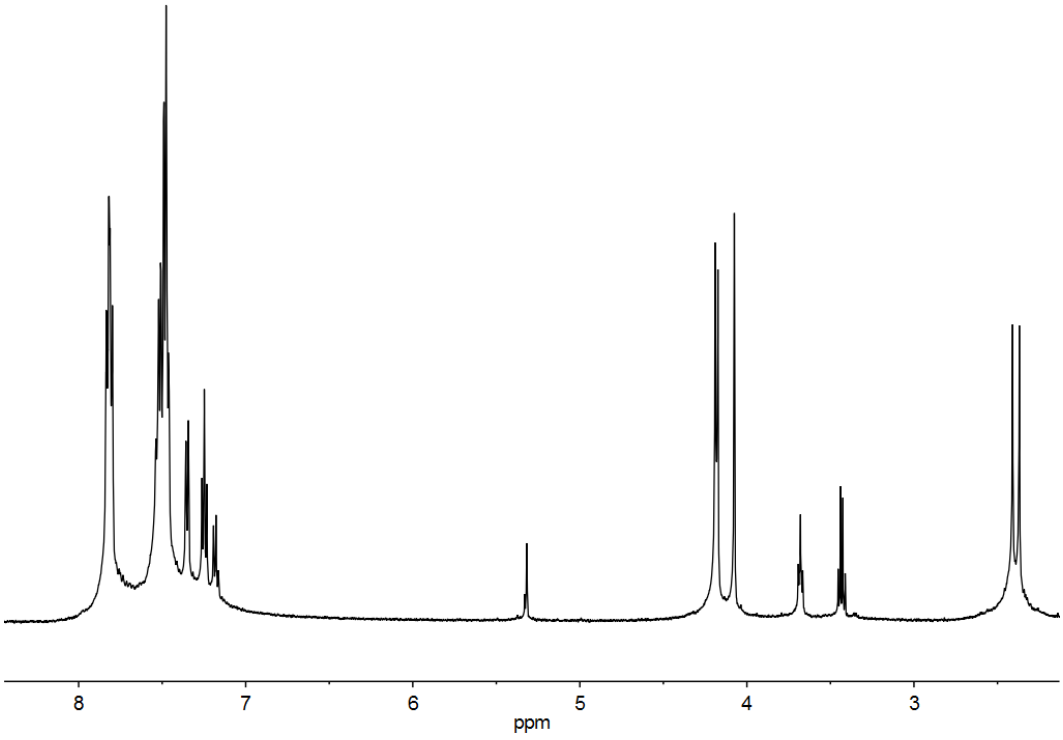

Figure S13. ^{1}H NMR spectrum (CD_2Cl_2, 500 MHz) of Pd[$(SCH_2)_2$NBn](dppe). The resonances at δ5.32, 3.69, and 3.43 are from $CHDCl_2$, THF, and Et_2O, respectively.

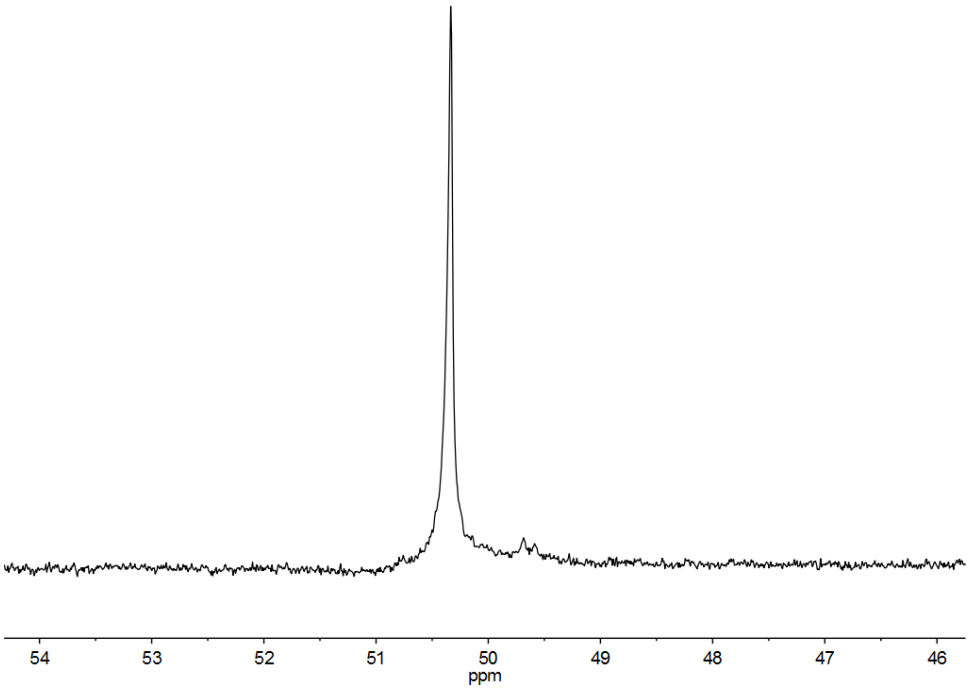

Figure S14. $^{31}P\{^{1}H\}$ NMR spectrum (CD_2Cl_2, 202 MHz) of Pd[$(SCH_2)_2$NBn](dppe).

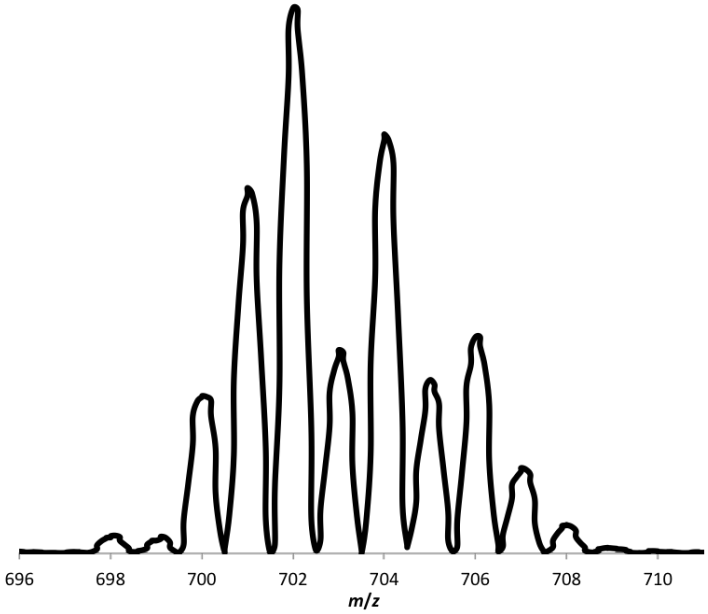

Figure S15. Positive ion ESI mass spectrum of Pd[$(SCH_2)_2$NBn](dppe).

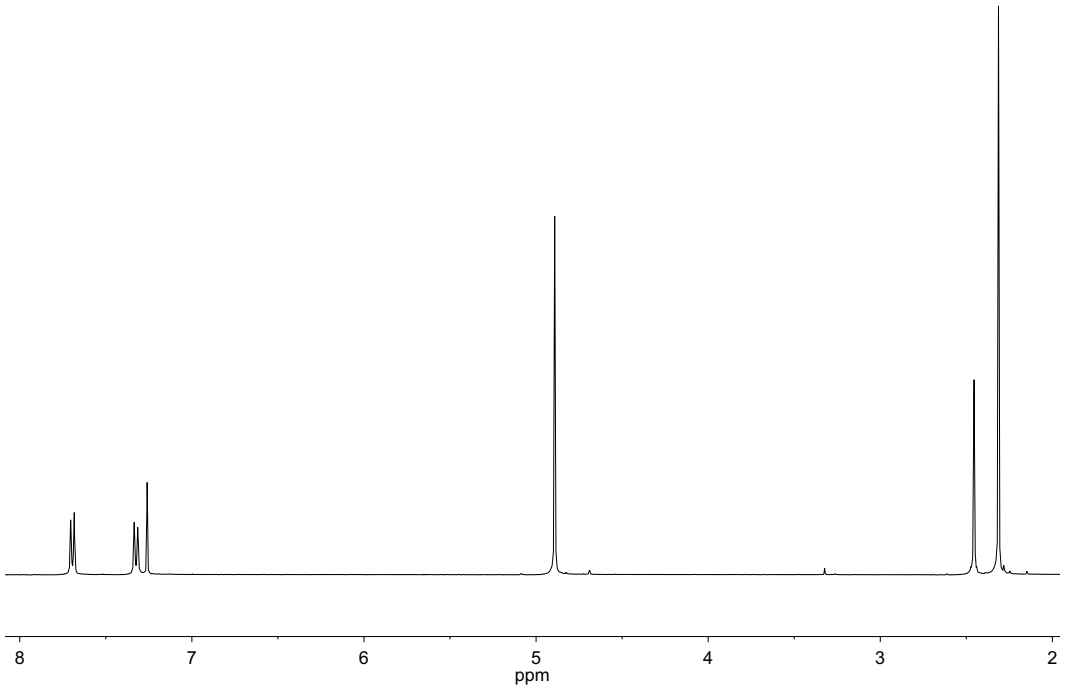

Figure S16. ^{1}H NMR spectrum ($CDCl_3$, 400 MHz) of $TsN(CH_2SAc)_2$. The resonance at δ7.26 is from $CDCl_3$.

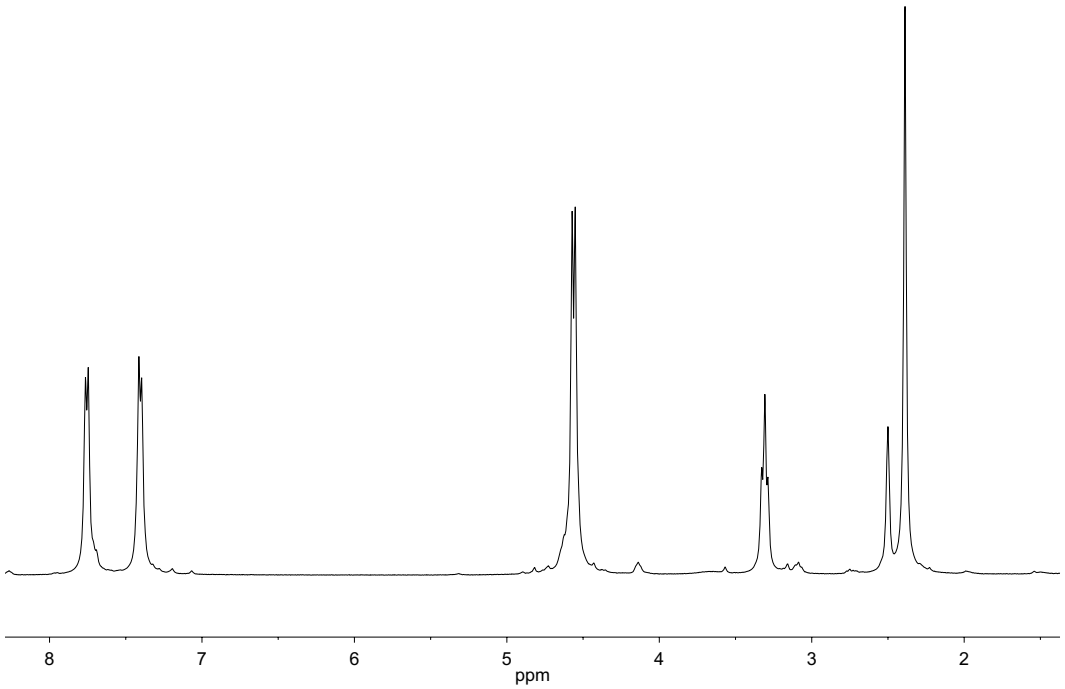

Figure S17. ^{1}H NMR spectrum (DMSO-d_6, 400 MHz) of $TsN(CH_2SH)_2$. The resonance at δ2.50 is from DMSO-d_5.

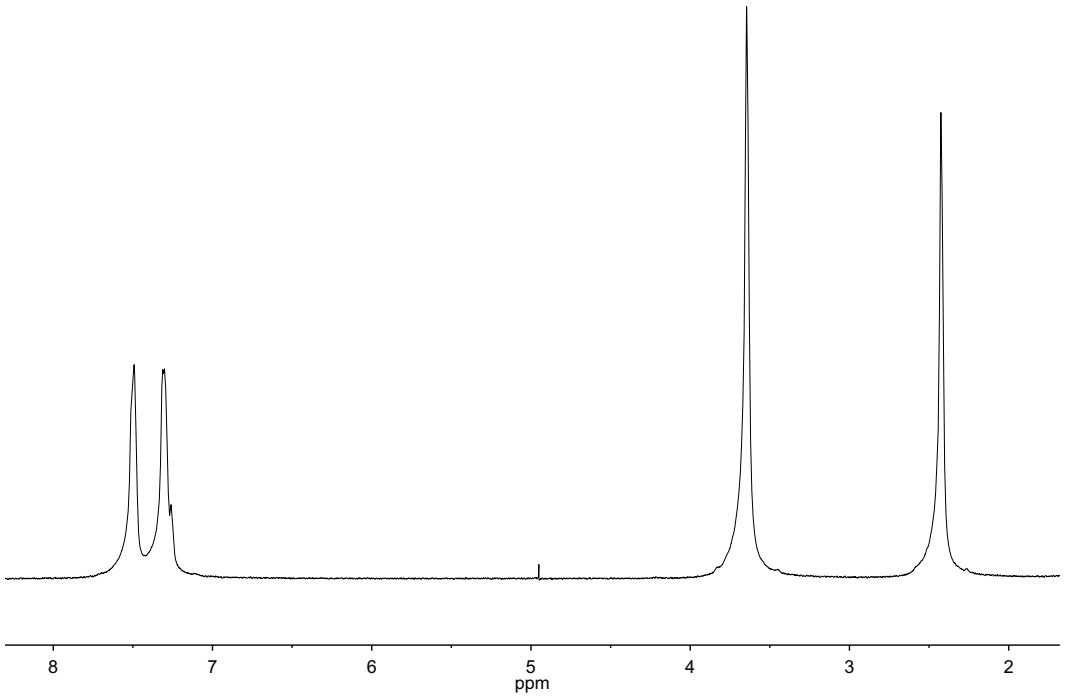

Figure S18. ^{1}H NMR spectrum ($CDCl_3$, 400 MHz) of $Fe_2[(SCH_2)_2NTs](CO)_6$. The resonance at δ7.26 is from $CDCl_3$.

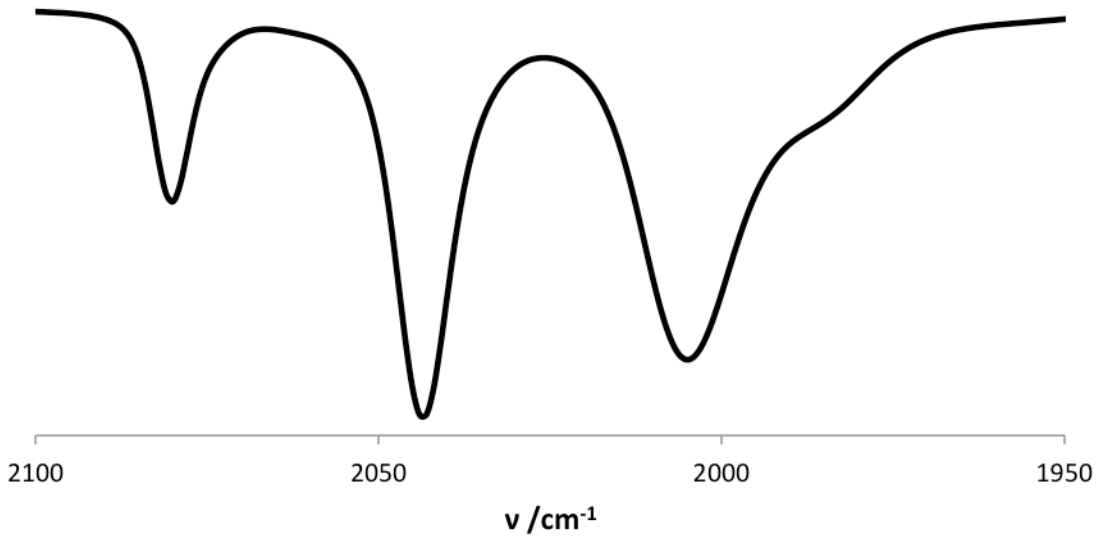

Figure S19. IR spectrum (CH_2Cl_2) of $Fe_2[(SCH_2)_2NTs](CO)_6$.

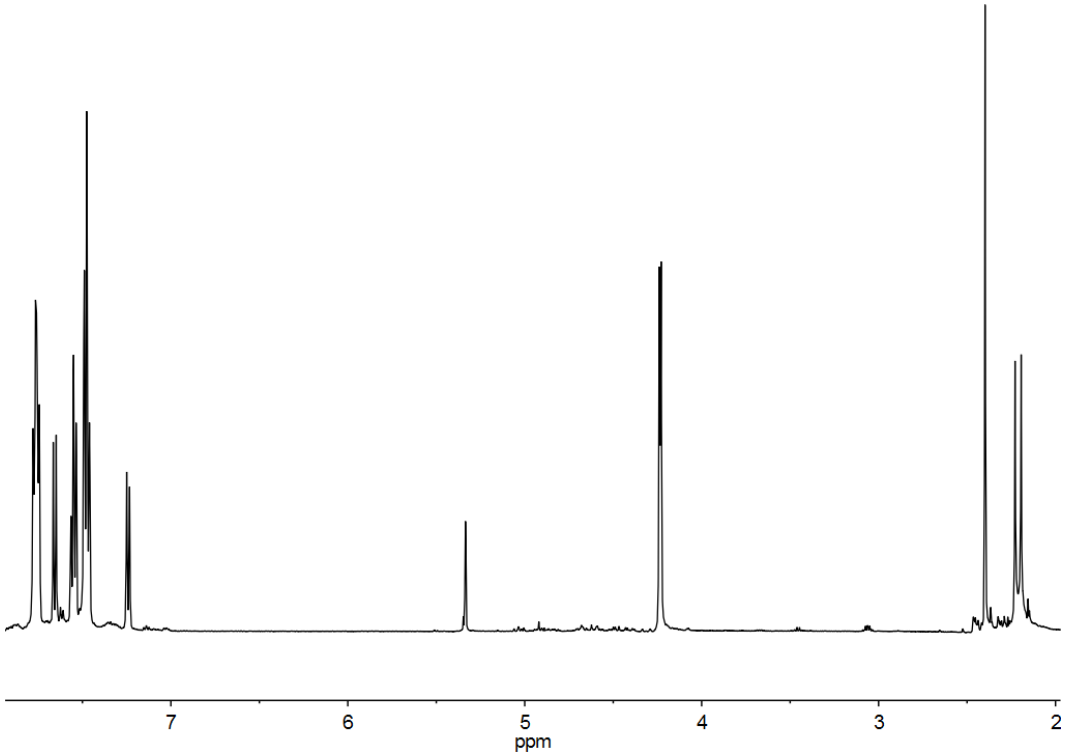

Figure S20. ^{1}H NMR spectrum (CD_2Cl_2, 500 MHz) of Ni[$(SCH_2)_2$NTs](dppe). The resonance at δ5.32 is from $CHDCl_2$.

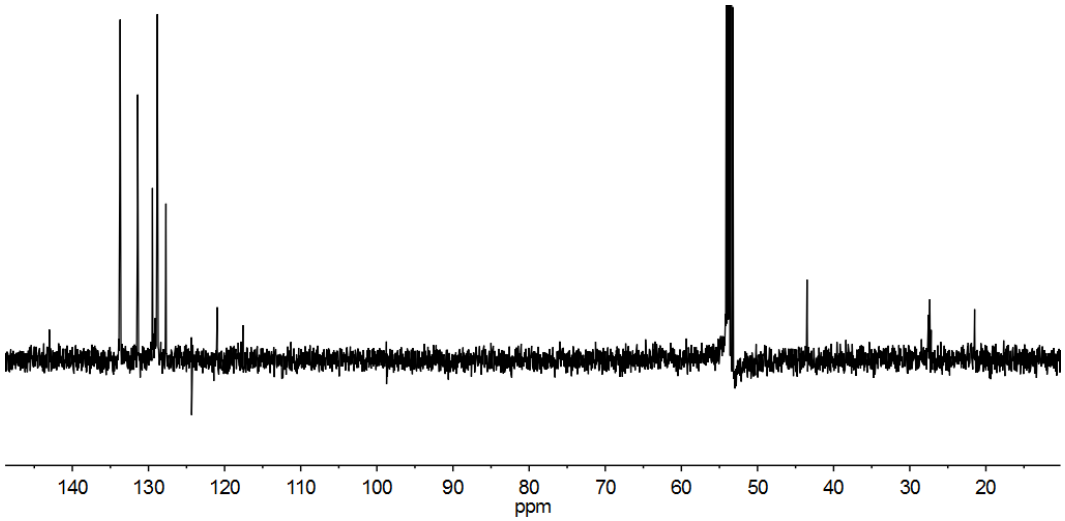

Figure S21. $^{13}C\{^{1}H\}$ NMR spectrum (CD_2Cl_2, 125 MHz) of Ni[$(SCH_2)_2$NTs](dppe).

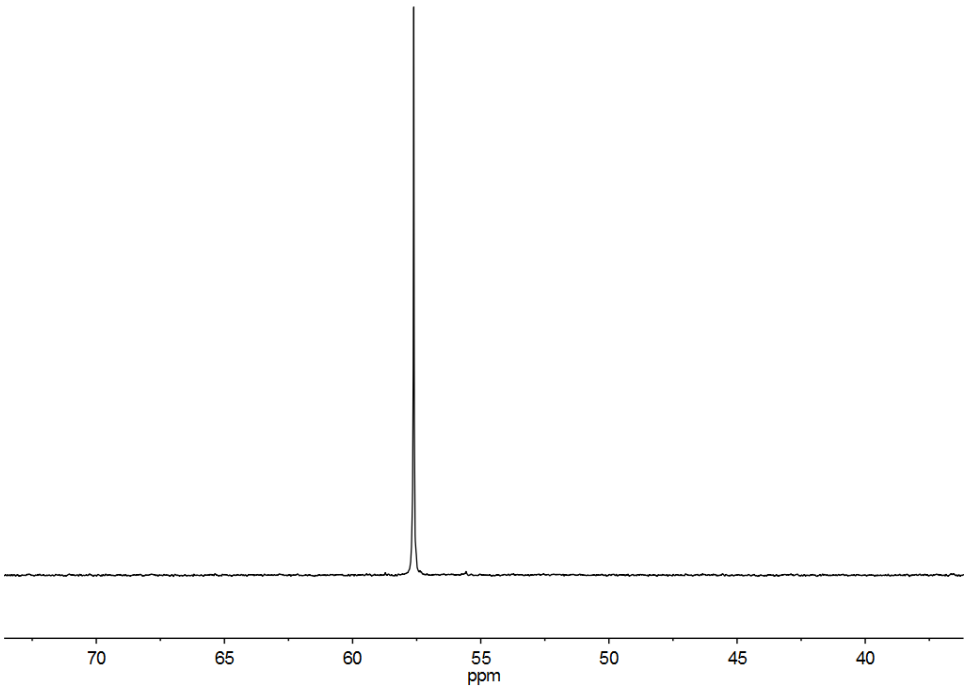

Figure S22. $^{31}P\{^{1}H\}$ NMR spectrum (CD_2Cl_2, 202 MHz) of Ni[$(SCH_2)_2$NTs](dppe).

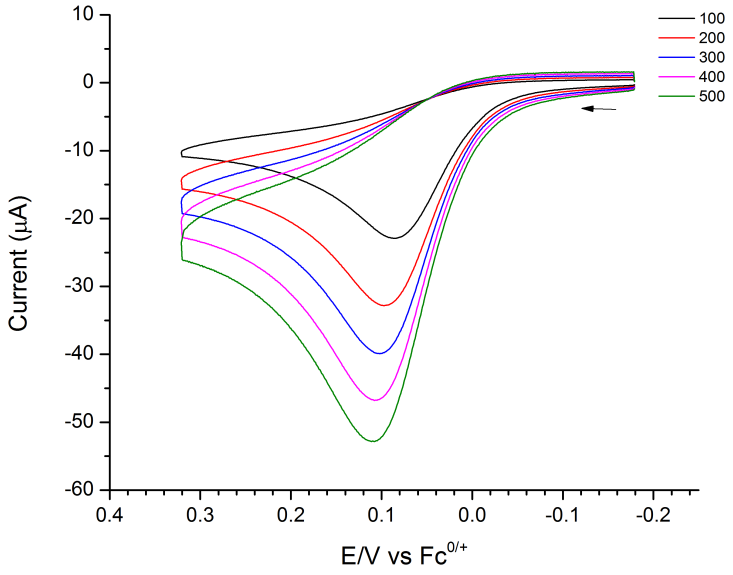

Figure S23. Cyclic voltammograms of $[Ni[(SCH_2)_2NBn](dppe)]^{0/+}$ at various scan-rates (mV/s). *Conditions:* 1 mM analyte and 0.1M $[Bu_4N]PF_6$ electrolyte in CH_2Cl_2 solution; glassy carbon working electrode, Ag/AgCl reference electrode, and Pt counter electrode.

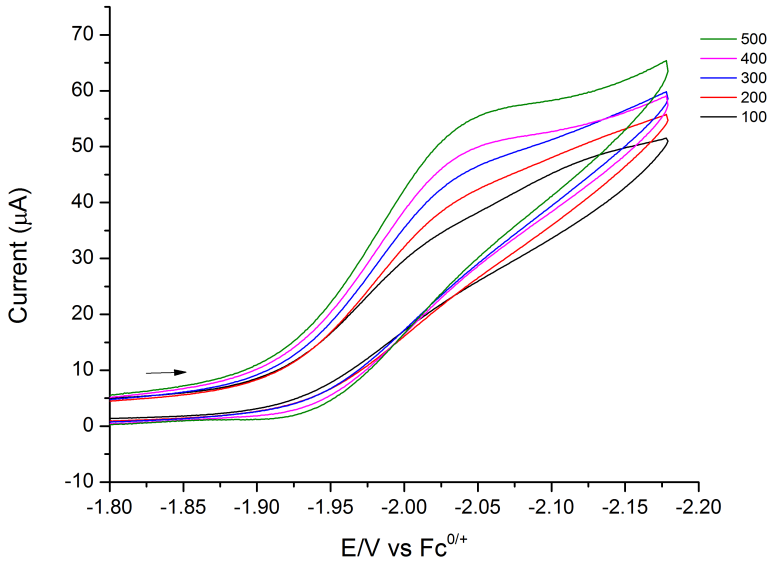

Figure S24. Cyclic voltammograms of $[Ni[(SCH_2)_2NBn](dppe)]^{0/-}$ at various scan rates (mV/s). *Conditions:* 1 mM analyte and 0.1 M $[Bu_4N][PF_6]$ electrolyte in CH_2Cl_2 solution; glassy carbon working electrode, Ag/AgCl reference electrode, and Pt counter electrode.

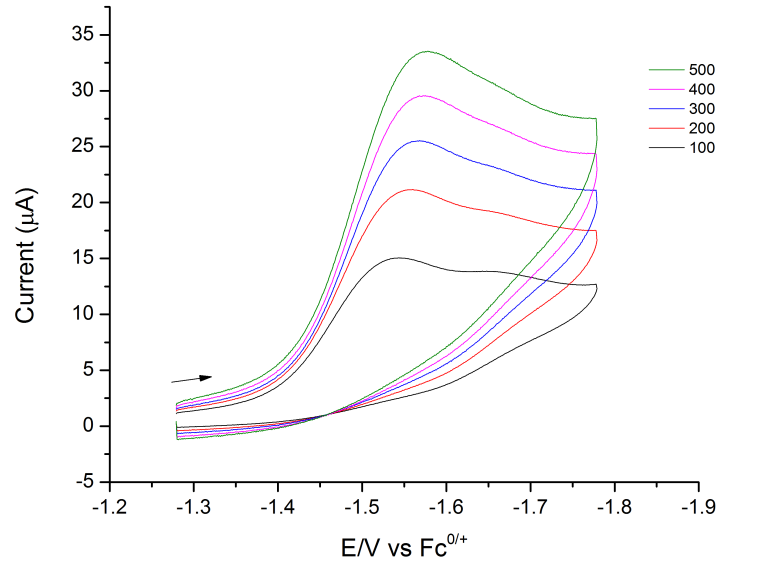

Figure S25. Cyclic voltammograms of $[Ni[(SCH_2)_2N(H)Bn](dppe)]^{+/0}$ at various scan rates (mV/s). *Conditions:* 1 mM analyte and 0.1 M $[Bu_4N]PF_6$ electrolyte in CH_2Cl_2; glassy carbon working electrode, Ag/AgCl reference electrode, and Pt counter electrode.

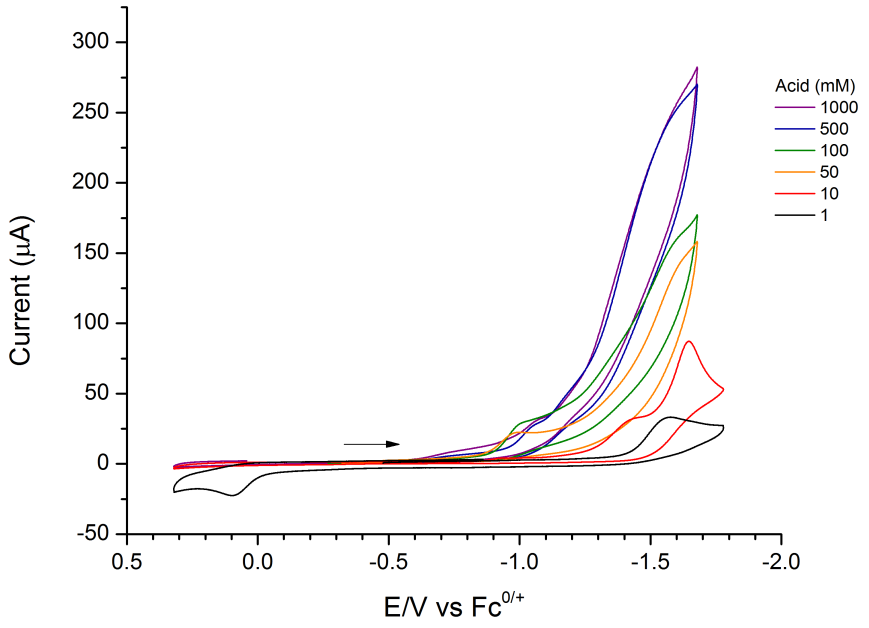

Figure S26. Cyclic voltammograms of $[Ni[(SCH_2)_2N(H)Bn](dppe)]^{+/0}$ with increasing concentrations of CF_3CO_2H. *Conditions:* 1 mM analyte and 0.1 M $[Bu_4N]PF_6$ electrolyte in CH_2Cl_2 solution; glassy carbon working electrode, Ag/AgCl reference electrode, and Pt counter electrode; 100 mV/s scan rate.

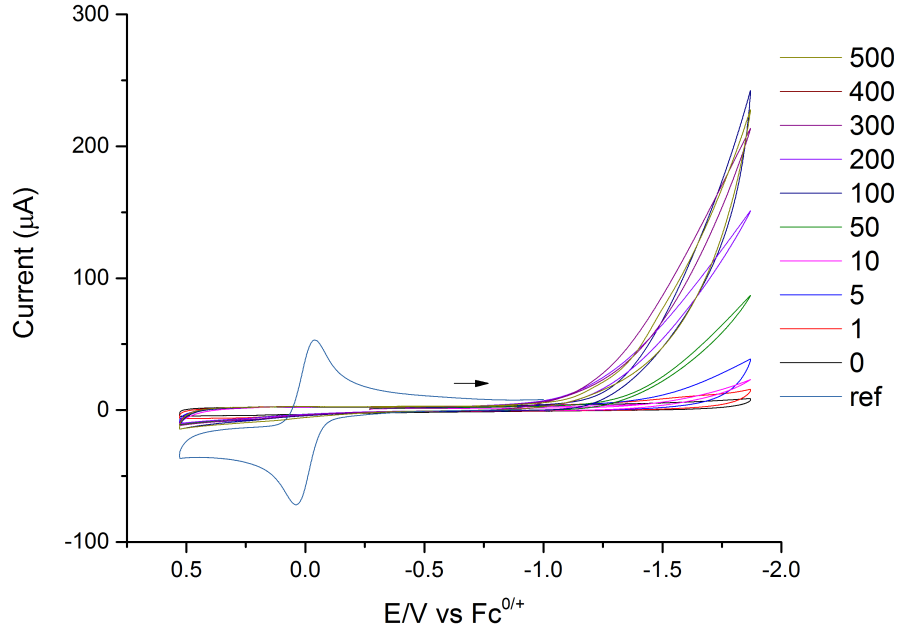

Figure S27. Cyclic voltammograms of CF_3CO_2H reduced by glassy carbon working electrode. *Conditions:* 0.1 M $[Bu_4N]PF_6$ electrolyte in CH_2Cl_2 solution, Ag/AgCl reference electrode, and Pt counter electrode; 100 mV/s scan rate. Fc was added as an internal reference after the last CV.

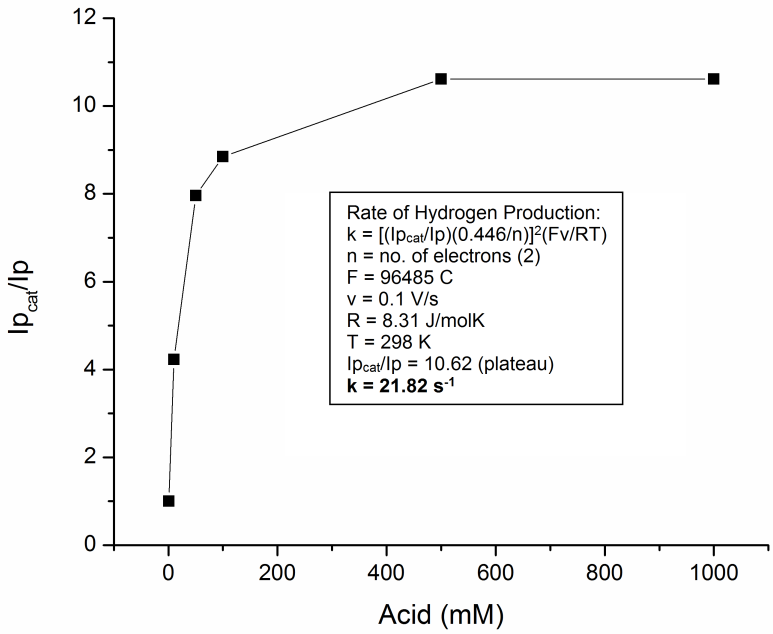

Figure S28. Plot of i_{pcat}/i_p of $[Ni[(SCH_2)_2NHBn](dppe)]^+$ (1 mM) versus $[CF_3CO_2H]$ added, where i_p is the current with 1 mM acid. *Inset:* rate calculation of hydrogen production from highest i_{pcat}/i_p values.

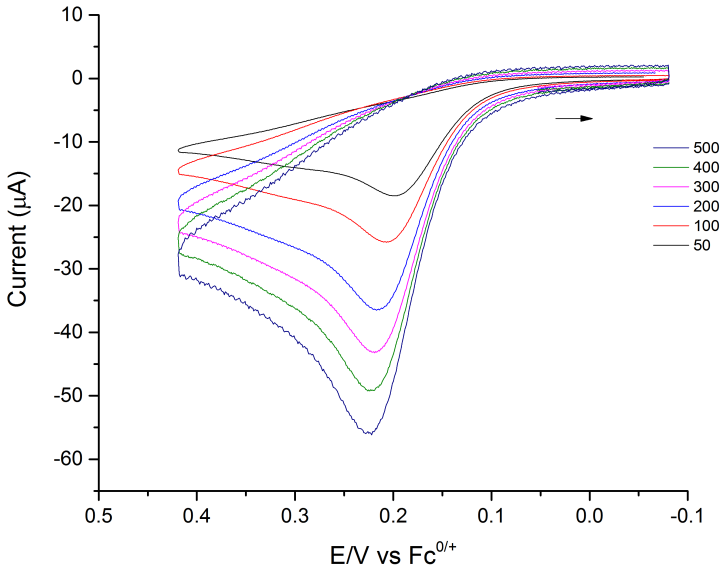

Figure S29. Cyclic voltammograms of $[Ni[(SCH_2)_2N(4\text{-}Cl\text{-}C_6H_4)]]^{0/+}$ at various scan-rates (mV/s). *Conditions:* 1 mM analyte and 0.1M $[Bu_4N]PF_6$ electrolyte in CH_2Cl_2 solution; glassy carbon working electrode, Ag/AgCl reference electrode, and Pt counter electrode.

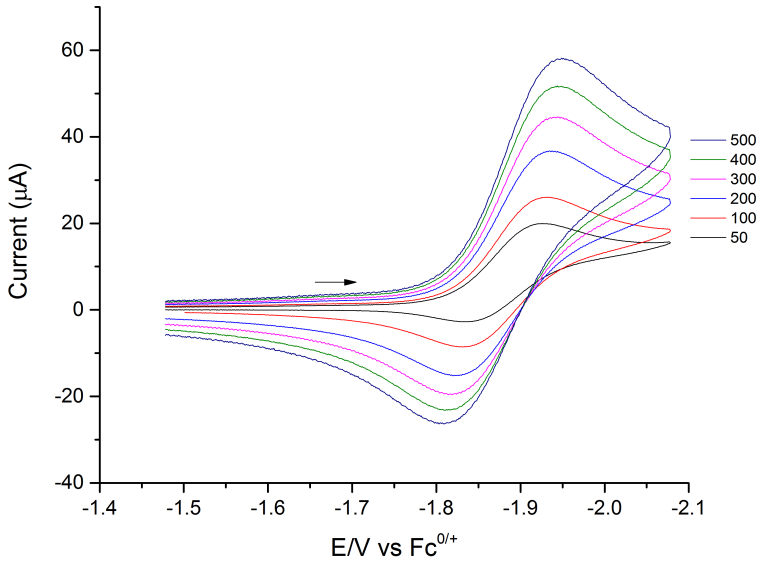

Figure S30. Cyclic voltammograms of $[Ni[(SCH_2)_2N(4\text{-}Cl\text{-}C_6H_4)]^{0/-}$ at various scan-rates (mV/s). *Conditions:* 1 mM analyte and 0.1M $[Bu_4N]PF_6$ electrolyte in CH_2Cl_2 solution; glassy carbon working electrode, Ag/AgCl reference electrode, and Pt counter electrode.